Electrocatalytic Production of H$_2$O$_2$ by Selective Oxygen Reduction Using Earth-Abundant Cobalt Pyrite (CoS$_2$)

Hongyuan Sheng,[†,§] Eric D. Hermes,[†,§] Xiaohua Yang,[†,‡,§] Diwen Ying,[†,#] Aurora N. Janes,[†] Wenjie Li,[†] J. R. Schmidt,*[,†] and Song Jin*[,†]

[†] Department of Chemistry, University of Wisconsin–Madison, 1101 University Avenue, Madison, Wisconsin 53706, United States

[‡] Key Laboratory of Ultrafine Materials of Ministry of Education, School of Materials Science and Engineering, East China University of Science and Technology, 130 Meilong Road, Shanghai 200237, China

[#] School of Environmental Science and Engineering, Shanghai Jiao Tong University, 800 Dongchuan Road, Shanghai 200240, China

[§] These authors contributed equally to this work.

*E-mail: schmidt@chem.wisc.edu
*E-mail: jin@chem.wisc.edu

SUPPORTING EXPERIMENTAL METHODS

Details for Materials Synthesis. The synthesis of CoS_2 nanomaterials and the direct growth of CoS_2 nanowires onto carbon fiber paper substrate (CoS_2/CFP) follow a published procedure with minor modifications.[S1] In a typical synthesis, 1.275 mmol of cobalt(II) chloride hexahydrate ($CoCl_2 \cdot 6H_2O$, Sigma-Aldrich, 98.0%) and 3 mmol of urea [$CO(NH_2)_2$, Riedel-de Haën, 99.5–100.5%] were dissolved in 75 mL of nanopure water, transferred into a 100-mL PTFE-lined stainless steel autoclave, sealed and heated at 120 °C for 5 h. Upon cooling to room temperature, the pink precipitates [cobalt hydroxide carbonate hydrate, $Co(OH)(CO_3)_{0.5} \cdot xH_2O$, CHCH] were washed with nanopure water and ethanol, collected by centrifuge and dried in a vacuum desiccator at room temperature. To convert CHCH nanomaterials into CoS_2 nanomaterials via thermal sulfidation, an alumina boat (CoorsTek) containing 50 mg of CHCH powders was placed in the center of a fused silica tube within a tube furnace (Lindberg/Blue M, TF55035A-1) with both pressure and gas flow controller, another alumina boat containing 2 g of sulfur (Sigma-Aldrich, 99.5–100.5%) was placed in the tube at the farthest upstream position within the tube furnace. The pressure in the tube was maintained at 780 Torr under a steady flow of Ar carrier gas (99.999%) at 25 sccm. The furnace temperature was quickly ramped from room temperature to 500 °C at a rate of approximately 80 °C/min and then held at 500 °C for 1 h, while the temperature of the sulfur boat was around 400 °C during thermal sulfidation. The tube furnace was then opened to allow natural cooling to room temperature under Ar flow, and the as-sulfidized CoS_2 nanomaterial product was stored in an Ar-filled glove box to minimize the exposure to air.

In a typical synthesis of CoS_2/CFP, Teflon-treated carbon fiber paper (Fuel Cell Earth, TGP-H-060) was first cleaned with oxygen plasma at 150 W power for 5 min (×2 for both sides) and further annealed in air at 700 °C for 5 min, resulting in improved surface wettability. 2.1 mmol of cobalt(II) nitrate hexahydrate [$Co(NO_3)_2 \cdot 6H_2O$, Sigma-Aldrich, ≥98.0%), 4.2 mmol of ammonium fluoride (NH_4F, Sigma-Aldrich, ≥98.0%), and 10.5 mmol of urea were dissolved in 80 mL of nanopure water, transferred into a 100-mL autoclave with a piece of annealed carbon fiber paper (3 cm × 6 cm) placed inside, and the sealed autoclave was heated at 110 °C for 5 h. Upon cooling to room temperature, the carbon fiber paper substrate covered with CHCH nanowires was sonicated in nanopure water (to remove loosely-bound CHCH powders), rinsed with nanopure

water and ethanol, and dried under N_2 flow. The subsequent thermal sulfidation was the same as mentioned above, except for replacing CHCH powders with the carbon fiber paper substrate covered with CHCH nanowires (which was cut into 1.5 cm × 6 cm for sulfidation). The as-sulfidized CoS_2/CFP was immersed in CS_2 to remove the excess sulfur and was then stored in an Ar-filled glove box to minimize the exposure to air. The catalyst loading of CoS_2/CFP was estimated by the mass difference of the CFP substrate before and after the growth of CoS_2 nanowires.

Sample Preparation for Materials Characterization. SEM samples of CoS_2 nanomaterials were prepared by drop-casting suspension of CoS_2 powders in ethanol onto Si wafer and drying under ambient condition. Graphite disk substrates were used for preparing the XPS samples of CoS_2 powders before and after ORR stability tests. Graphite disk substrate was made by cutting thin slices of graphite rod (Ultra Carbon Corp., Ultra "F" Purity), abrading both sides with 600-grit silicon carbide paper (Allied High Tech Products, Inc.), and sonicating in nanopure water and ethanol until clean. To prepare the XPS samples, the as-synthesized CoS_2 powders were dispersed in nanopure water and drop-casted on graphite disk substrates, while the CoS_2 powders after ORR stability tests were first recovered from the electrodes by sonicating in nanopure water and ultracentrifuging at 13.2K rpm for 1 min, followed by re-dispersing in minimal amount of nanopure water and drop-casting on graphite disk substrates. The XPS samples were used for Raman experiments without modification.

Detailed Protocols for Calibrating the Collection Efficiency of RRDE. Calibration of the collection efficiency was performed on the bare RRDE. The electrolyte was prepared by dissolving 4 mM of potassium ferricyanide(III) ($K_3[Fe(CN)_6]$, Sigma-Aldrich, 99%) in 0.05 M Na_2SO_4. The electrolyte was purged with Ar gas for at least 15 min prior to the measurements in order to eliminate dissolved O_2 gas. A blanket of Ar gas was maintained over the surface of the electrolyte during the measurements.

(a) Cyclic voltammetry (CV) was performed separately on the disk and the ring between 0 V and 1.23 V vs. RHE at 100 mV/s and 0 rpm (Figure S4a shows the CV voltammogram of the disk).

(b) Linear sweep voltammetry (LSV) was performed on the disk from 1.23 V to 0 V vs. RHE at 50 mV/s and 1600 rpm, meanwhile the ring was held at 1.20 V vs. RHE. Ferricyanide reduction on the bare GC disk was found to be diffusion-limited at 0 V vs. RHE.

(c) LSV was performed on the ring from 0 V to 1.23 V vs. RHE at 50 mV/s and 1600 rpm, meanwhile the disk was held at 0 V vs. RHE. Ferrocyanide oxidation on the Pt ring was found to be diffusion-limited at 1.20 V vs. RHE (Figure S4b).

(d) RRDE voltammograms were recorded by performing LSV on the disk from 1.23 V to 0 V vs. RHE at 50 mV/s and different rotation rates (400, 625, 900, 1225, 1600, and 2025 rpm), meanwhile the ring was held at 1.20 V vs. RHE (Figure S4c). The collection efficiency (N) of RRDE is calculated using the equation:

$$N = \frac{i_{ring}}{i_{disk}}$$

where i_{ring} and i_{disk} are the ring and the disk current, respectively. When both ferricyanide reduction on the bare GC disk and ferrocyanide oxidation on the Pt ring became diffusion-limited, the collection efficiency was found to be 0.43 and was independent of the RRDE rotation rate (Figure S4d).

Detailed Protocols for ORR Measurements of Pt/C and Vulcan Carbon Black. The electrolyte (0.05 M H_2SO_4 or 0.05 M Na_2SO_4) was purged with Ar gas for at least 15 min prior to the measurements in order to eliminate dissolved O_2 gas. A blanket of Ar gas was maintained over the surface of the electrolyte during the measurements.

(a) 5 mg of 20 wt% Pt/C (Sigma-Aldrich) or Vulcan XC72R carbon black (Cabot Corp.) was suspended in 250 μL of Nafion solution (Sigma-Aldrich, 5 wt% in lower aliphatic alcohols and water) and 2250 μL of nanopure water by sonicating for 1 h, then 10 μL of the suspension was drop-casted onto the disk of RRDE and dried under ambient condition at a rotation rate of 700 rpm to achieve a uniform catalyst film.

(b) The Pt/C- or Vulcan-casted disk was first conditioned in Ar-saturated electrolyte by performing CV between 0.05 V and 1.20 V vs. RHE (without iR-correction) at 100 mV/s and 1600 rpm for 50 cycles, meanwhile the Pt ring was held at 0.70 V vs. RHE.

(c) The Pt ring was conditioned in Ar-saturated electrolyte by performing CV between 0.05 V and 1.20 V vs. RHE (without *iR*-correction) at 100 mV/s and 1600 rpm for 50 cycles, meanwhile the Pt/C- or Vulcan-casted disk was held at 0.70 V vs. RHE.

(d) For background current measurements, LSV of the Pt/C-casted disk was swept in positive direction from 0 to 1.2 V vs. RHE (without *iR*-correction) at 50 mV/s and 400 rpm, LSV of the Vulcan-casted disk was swept in negative direction from 1.2 to 0 V vs. RHE (without *iR*-correction) at 50 mV/s and 400 rpm.

(e) The electrolyte was then saturated with O_2 gas for ORR measurements. The Pt/C- or Vulcan-casted disk was conditioned in O_2-saturated electrolyte by performing CV between 0.05 V and 1.20 V vs. RHE (without *iR*-correction) at 100 mV/s and 1600 rpm for 10 cycles, meanwhile the Pt ring was held at 1.3 V vs. RHE.

(f) The Pt ring was conditioned in O_2-saturated electrolyte by performing CV between 0.05 V and 1.20 V vs. RHE (without *iR*-correction) at 100 mV/s and 1600 rpm for 10 cycles, meanwhile the Pt/C- or Vulcan-casted disk was held at 1.2 V vs. RHE.

(g) To record RRDE voltammograms in O_2-saturated electrolyte, LSV of the Pt/C-casted disk was swept in positive direction from 0 to 1.2 V vs. RHE (without *iR*-correction) at 50 mV/s and different rotation rates, LSV of the Vulcan-casted disk was swept in negative direction from 1.2 to 0 V vs. RHE (without *iR*-correction) at 50 mV/s and different rotation rates, meanwhile the Pt ring was held at 1.3 V vs. RHE. The H_2O_2 selectivity (p) and the electron transfer number (n) is calculated using the following equations:

$$p = 2 \times \frac{\dfrac{i_{ring}}{N}}{i_{disk} + \dfrac{i_{ring}}{N}}$$

$$n = 4 \times \frac{i_{disk}}{i_{disk} + \dfrac{i_{ring}}{N}}$$

where i_{disk} and i_{ring} are the disk and the ring current, respectively, and N is the collection efficiency determined above (0.43). We note that, for the ease of directly visualizing the H_2O_2 selectivity from the RRDE voltammograms (Figure S5a, S5c, S6a, S6c), both the disk and the ring current densities are presented based on the geometric area of the disk electrode (0.126 cm^2), and the ring current density is further adjusted by collection efficiency:

$$j_{disk} = \frac{i_{disk}}{A_{disk}}$$

$$j_{ring} = \frac{i_{ring}}{A_{disk} \times N} = j_{peroxide}$$

where $j_{peroxide}$ is the partial disk current density that produces hydrogen peroxide (i.e., the hydrogen peroxide current density). Besides the RRDE method described above, the electron transfer number (n) can also be calculated based on the Koutecky-Levich (K-L) method that describes the behavior of the disk current density:

$$\frac{1}{j_{disk}} = \frac{1}{j_k} + \frac{1}{j_L}$$

$$j_L = 0.62 \times n \times F \times D^{2/3} \times v^{-1/6} \times C^* \times \omega^{1/2}$$

$$\frac{1}{j_{disk}} = \frac{1}{j_k} + \frac{1}{0.62 \times n \times F \times D^{2/3} \times v^{-1/6} \times C^*} \times \omega^{-1/2}$$

where j_k and j_L are the kinetic and diffusion-limited current density, respectively, F is the Faraday constant, D is the diffusion coefficient of O_2, v is the kinematic viscosity of the electrolyte, C^* is the concentration of O_2 in the bulk electrolyte, and ω is the angular velocity (in rad/s) of the disk electrode. Thus, n can be deduced from and should be inversely proportional to the slope of the linear plot of $\frac{1}{j_{disk}}$ vs. $\omega^{-1/2}$.

(f) The uncompensated resistance (R_u) was finally measured using electrochemical impedance spectroscopy (EIS). EIS measurement was performed on the CoS$_2$-casted disk (held at open circuit potential) over the frequency range from 100 kHz to 100 mHz. R_u could be estimated at the high-frequency region of the EIS spectrum where the phase angle is closest to 0°.[S2] The magnitude of R_u was dependent of the electrolyte (around 50 Ω in 0.05 M H$_2$SO$_4$ and around 130 Ω in 0.05 M Na$_2$SO$_4$). For all the RRDE voltammograms of Pt/C and Vulcan carbon black recorded in O$_2$-saturated electrolyte (Figure S5, S6), iR-correction was manually performed after subtracting background current.

Detailed Protocols for ORR Measurements of Drop-Casted CoS$_2$. The electrolyte (0.05 M H$_2$SO$_4$ or 0.05 M Na$_2$SO$_4$) was purged with O$_2$ gas for at least 15 min prior to the measurements in order to reach a saturated concentration of dissolved O$_2$ gas. During the measurements, a blanket

of O_2 gas was maintained over the surface of the electrolyte to ensure that the concentration of dissolved O_2 gas remained stable.

(a) The CoS_2-casted disk was conditioned in O_2-saturated electrolyte by performing CV between -0.025 V and 0.80 V vs. RHE (without *iR*-correction) at 100 mV/s and 1600 rpm for 10 cycles, meanwhile the Pt ring was held at 1.3 V vs. RHE.

(b) The Pt ring was conditioned in O_2-saturated electrolyte by performing CV between 0.05 V and 1.20 V vs. RHE (without *iR*-correction) at 100 mV/s and 1600 rpm for 10 cycles, meanwhile the CoS_2-casted disk was held at 0.80 V vs. RHE.

(c) To record RRDE voltammograms in O_2-saturated electrolyte, LSV of the CoS_2-casted disk was performed from 0.80 V to -0.025 V vs. RHE (without *iR*-correction) at 50 mV/s and different rotation rates, meanwhile the Pt ring was held at 1.3 V vs. RHE.

(d) The electrolyte was then saturated with Ar gas for background current measurements. LSV was performed on the CoS_2-casted disk from 0.80 V to -0.025 V vs. RHE (without *iR*-correction) at 50 mV/s and 400 rpm.

(e) The electrochemically active surface area (ECSA) of the CoS_2-casted disk was determined by performing CV at different scan rates between -0.025 V and 0.80 V vs. RHE (without *iR*-correction) in Ar-saturated electrolyte.

(f) The uncompensated resistance (R_u) was finally measured using electrochemical impedance spectroscopy (EIS) For all the RRDE voltammograms of CoS_2 recorded in O_2- and Ar-saturated electrolyte (Figure 2, S7, S8, S10 to S12, S14 to S16), *iR*-correction was manually performed after subtracting background current.

Detailed Protocols for Bulk ORR Electrolysis on Integrated CoS_2/CFP Electrode and Chemical Quantification of H_2O_2 Product. For bulk ORR electrolysis, CoS_2 nanowires directly grown on carbon fiber paper (CoS_2/CFP) was used as the working electrode to achieve a larger catalytic current and therefore a higher H_2O_2 yield. To prepare working electrodes of CoS_2/CFP, 5-minute epoxy (Devcon) was used to define the geometric area of the working electrodes to about 1 cm $\times$ 1 cm (Figure S19a). A three-electrode H-cell setup was used to avoid the oxidation of H_2O_2 product on the counter electrode, and a minimal volume (3 mL) of electrolyte was filled into the working electrode compartment to obtain higher concentrations of H_2O_2 (Figure S19b).

(a) To prepare for ORR electrolysis in a three-electrode H-cell, Nafion 117 membrane (Sigma-Aldrich) was cut into circular pieces (with appropriate diameter to cover the junction of H-cell), cleaned by immersing into 3 wt% H_2O_2, nanopure water, 1 M H_2SO_4, and nanopure water (at 80 °C for 1 h for each step), and stored in 0.05 M H_2SO_4 at room temperature before use. The graphite rod counter electrode was separated from the CoS_2/CFP working electrode and the $Hg/HgSO_4$ (saturated K_2SO_4) reference electrode by Nafion membrane. The electrolyte (0.05 M H_2SO_4) was purged with O_2 gas for at least 15 min prior to the measurements in order to reach a saturated concentration of dissolved O_2 gas, a blanket of O_2 gas was maintained over the electrolyte during the measurements to ensure that the concentration of dissolved O_2 gas remained stable.

(b) To figure out the operating conditions of ORR electrolysis, we performed CV on CoS_2/CFP between -0.025 V and 0.80 V vs. RHE (without *iR*-correction) at 100 mV/s in O_2-saturated 0.05 M H_2SO_4 and found that vigorous stirring the electrolyte enhanced the catalytic current by facilitating the mass transport of O_2 (Figure S20a, S20b). Therefore, we performed ORR electrolysis at the maximum stir rate (1200 rpm) of the stir plate used. We also performed control experiments to confirm that plain CFP was inert towards ORR in 0.05 M H_2SO_4 (Figure S20c, S20d). We chose 0.5 V vs. RHE as the working electrode potential for ORR electrolysis because the RRDE results suggested the H_2O_2 production at high catalyst loadings peaked around 0.5 V vs. RHE (Figure 3b). Note that R_u became much smaller in the H-cell (1 to 3 Ω for 0.05 M H_2SO_4) compared with that in the RRDE cell since the reference electrode can be much closer to the surface of the working electrode in the H-cell setup.

(c) The ceric sulfate titration of H_2O_2 follows the reaction: $2\ Ce^{4+} + H_2O_2 \rightarrow 2\ Ce^{3+} + 2\ H^+ + O_2$; Ce^{4+} has a peak absorbance at 319 nm while Ce^{3+} is colorless, the reduction of Ce^{4+} to Ce^{3+} by H_2O_2 results in a decrease in the absorbance. Note that Ce^{4+} is only soluble in highly acidic solution due to its strong tendency to hydrolyze. Therefore, anhydrous $Ce(SO_4)_2$ (Sigma-Aldrich) was dissolved in 0.5 M H_2SO_4 to prepare a series of standard Ce^{4+} solutions (up to 0.5 mM). Absorption spectroscopy of standard Ce^{4+} solutions was performed on a JASCO V-570 UV/Vis/NIR spectrophotometer at 319 nm, and a calibration curve was generated (Figure S22a and inset).

$$Abs = \varepsilon \times l \times [Ce^{4+}]$$

where *Abs* is the absorbance at 319 nm, $[Ce^{4+}]$ is the Ce^{4+} concentration (mM), ε is the molar absorptivity of Ce^{4+} ($mM^{-1}\ cm^{-1}$), and *l* is the path length (1 cm).

(d) Before performing ORR electrolysis on CoS$_2$/CFP in 0.05 M H$_2$SO$_4$, CV was first performed on CoS$_2$/CFP between -0.025 V and 0.80 V vs. RHE (without *iR*-correction) at 100 mV/s to condition the working electrode (10 cycles each at the stir rate of 0 rpm and 1200 rpm). A 50-µL aliquot of the working electrode compartment electrolyte was sampled and injected into 4 mL of 0.422 mM Ce^{4+} stock solution in 0.5 M H$_2$SO$_4$, which allows for calculating the initial H$_2$O$_2$ concentration in the electrolyte before the ORR electrolysis started:

$$[Ce^{4+}]_{before} = \frac{Abs_{before}}{\varepsilon \times l}$$

$$[Ce^{4+}]_{after} = \frac{Abs_{after}}{\varepsilon \times l}$$

$$H_2O_2 \text{ concentration (mM) in the 50-µL aliquot} = \frac{4 \times [Ce^{4+}]_{before} - 4.05 \times [Ce^{4+}]_{after}}{2 \times 0.05}$$

where Abs_{before} and Abs_{after} are the absorbances of Ce^{4+} stock solution at 319 nm before and after injecting H$_2$O$_2$-containing aliquot. Note that (1) the initial concentration of Ce^{4+} stock solution, $[Ce^{4+}]_{before}$, does not need to be exact and can always be found using the calibration curve; (2) H$_2$O$_2$ always need to be the limiting reagent when reacting with Ce^{4+} stock solution so that $[Ce^{4+}]_{after} > 0$; (3) Ce^{4+} stock solution should remain almost the same acidic pH after aliquot injection to avoid cerium hydroxides precipitate out at higher pH.[S3]

(e) We then carried out ORR electrolysis on CoS$_2$/CFP in 0.05 M H$_2$SO$_4$ at 0.5 V vs. RHE and 1200 rpm stir rate for 60 min, with eight 50-µL aliquots of the working electrode compartment electrolyte sampled at 5, 10, 15, 20, 30, 40, 50, and 60 min after electrolysis started. The volume of the electrolyte left in the working electrode compartment at the end of electrolysis was 2.55 mL. The relationships among cumulative H$_2$O$_2$ yield, H$_2$O$_2$ selectivity, and Faradaic efficiency can be described by the following equations:

$$\text{Cumulative Faradaic efficiency (\%)} = 100 \times \frac{2 \times 96485 \times \text{Cumulative H}_2\text{O}_2 \text{ yield (mol)}}{\int_0^t I\, dt}$$

$$\text{Cumulative H}_2\text{O}_2 \text{ selectivity (\%)} = \frac{200}{1 + \dfrac{\int_0^t I\, dt}{2 \times 96485 \times \text{Cumulative H}_2\text{O}_2 \text{ yield (mol)}}}$$

$$\text{Cumulative H}_2\text{O}_2 \text{ selectivity (\%)} = \frac{200}{1 + \dfrac{100}{\text{Cumulative Faradaic efficiency (\%)}}}$$

where $\int_0^t I\, dt$ stands for the cumulative charge passed (C) during electrolysis.

Detailed Protocols for Examining the Chemical Stability of Nonstabilized H_2O_2 Under Different pH Conditions. 0.03 wt% H_2O_2 aqueous solutions in 0.5 M H_2SO_4 (pH 0.5), in 0.5 M Na_2SO_4 with 1.6 mM H_2SO_4 (pH 3.3), in 0.5 M Na_2SO_4 with 1.6 mM NaOH (9.3), and in 0.1 M NaOH (pH 12.7) were prepared from the following chemicals: 30 wt% H_2O_2 (Acros Organics, nonstabilized in water), H_2SO_4 (Sigma-Aldrich, 95.0-98.0%), Na_2SO_4 (Sigma-Aldrich, $\geqslant$99.0%), NaOH (Sigma-Aldrich, semiconductor grade, 99.99% trace metals basis), and nanopure water. These 0.03 wt% H_2O_2 aqueous solutions were kept at room temperature and ambient pressure in sealed polypropylene centrifuge tubes (VWR Superclear Ultra High Performance). The concentration of H_2O_2 in these 0.03 wt% H_2O_2 aqueous solutions were periodically quantified on a daily basis over the time period of one week using the ceric sulfate titration method described above.

SUPPORTING FIGURES AND TABLES
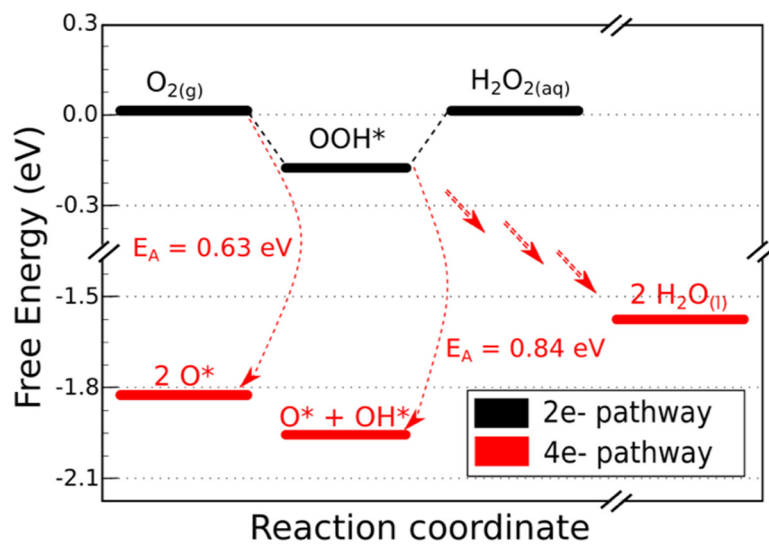
Figure S1. Free energy diagram for both two-electron (2e⁻) and four-electron (4e⁻) ORR on the CoS₂ (100) surface at the calculated standard equilibrium reduction potential of 2e⁻ ORR with the PBE-D3(ABC) dispersion-corrected density functional method.
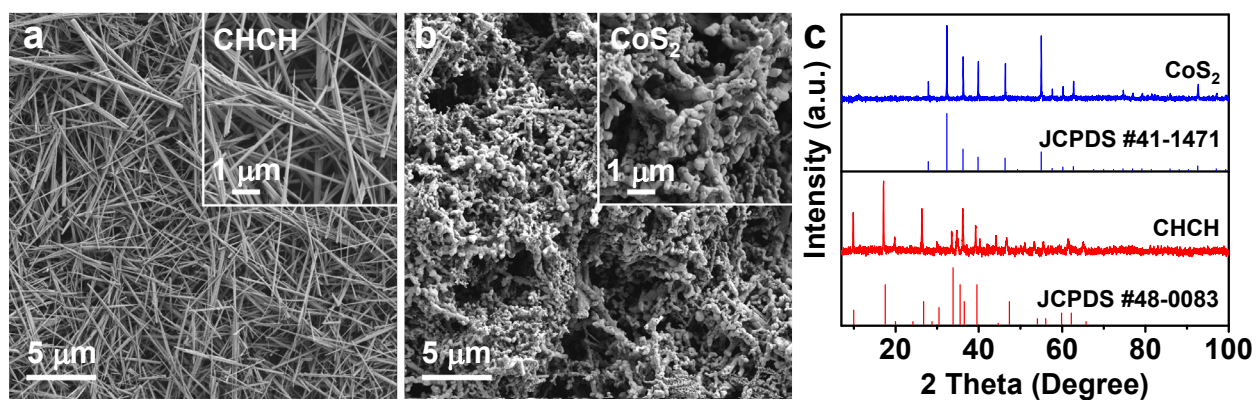
Figure S2. SEM images of (a) CHCH and (b) CoS$_2$ nanomaterial powders. (c) PXRD patterns of CHCH and CoS$_2$ powders in comparison with the standard PXRD patterns of CHCH (JCPDS #48-0083) and CoS$_2$ (JCPDS #41-1471).
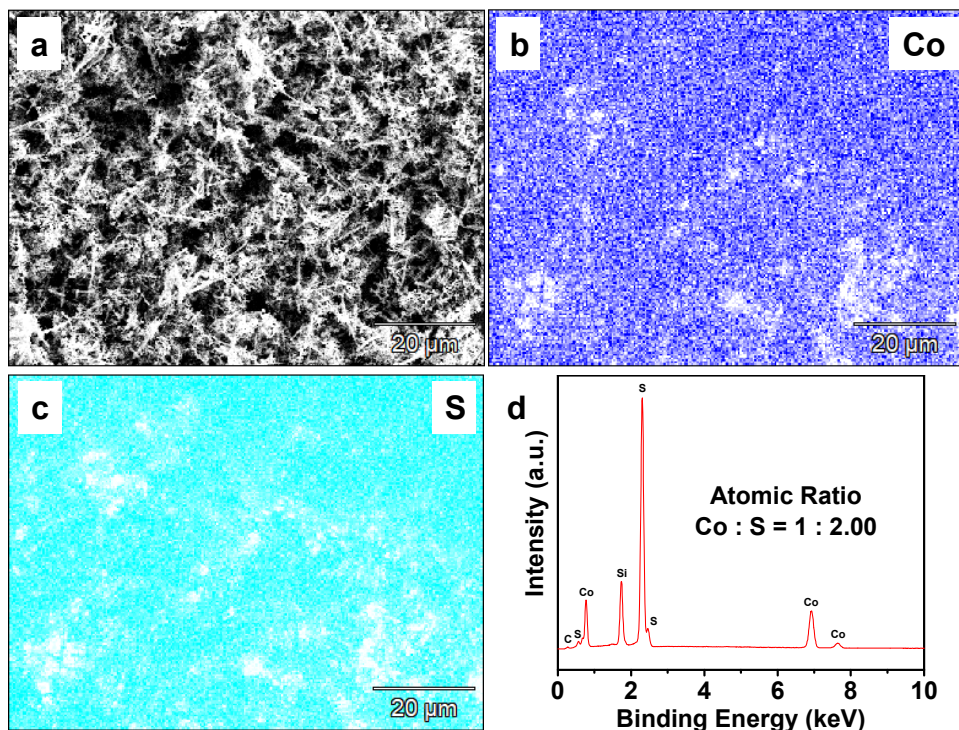
Figure S3. (a) SEM image, (b,c) EDS elemental maps, and (d) EDS spectrum of CoS$_2$ powders.
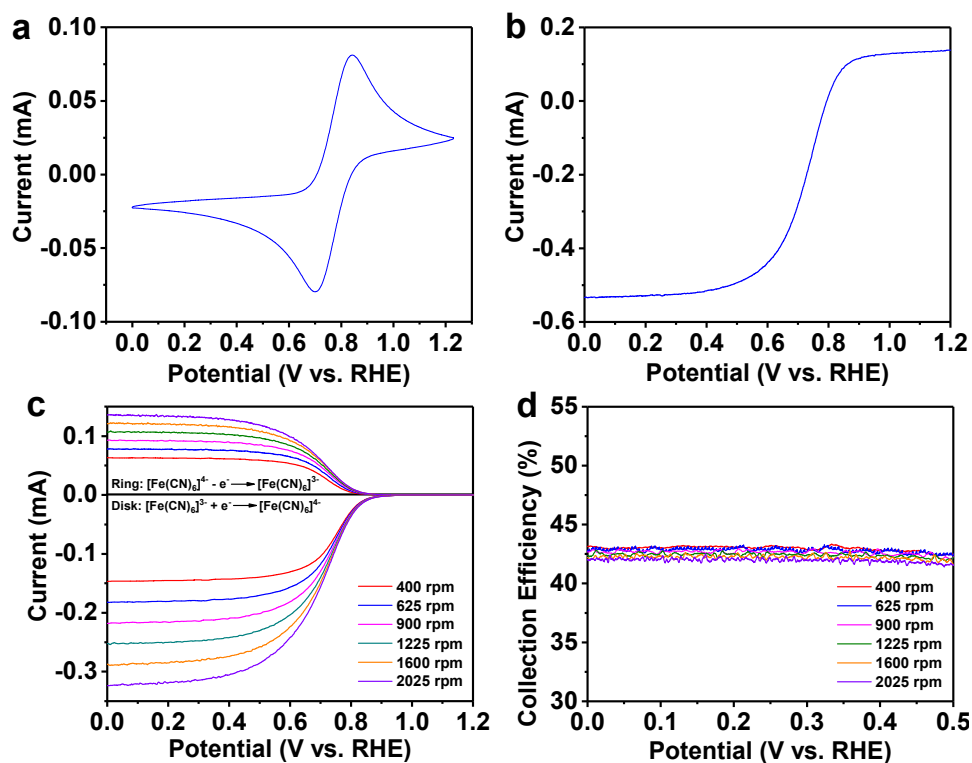
Figure S4. Calibration of the collection efficiency of the bare RRDE in Ar-saturated 0.05 M Na$_2$SO$_4$ dissolved with 4 mM of K$_3$[Fe(CN)$_6$]. (a) CV voltammogram of the bare GC disk of RRDE at 100 mV/s and 0 rpm, (b) LSV voltammogram of the Pt ring from 0 V to 1.23 V vs. RHE at 50 mV/s and 1600 rpm while holding the GC disk at 0 V vs. RHE, (c) RRDE voltammograms recorded at different rotation rates by performing LSV on the disk from 1.23 V to 0 V vs. RHE at 50 mV/s while holding the ring at 1.20 V vs. RHE, (d) the corresponding collection efficiency of RRDE voltammograms as a function of the potential. All potentials in this figure are presented without *iR*-correction (R_u for the bare GC disk is 130.2 Ω in this experiment).
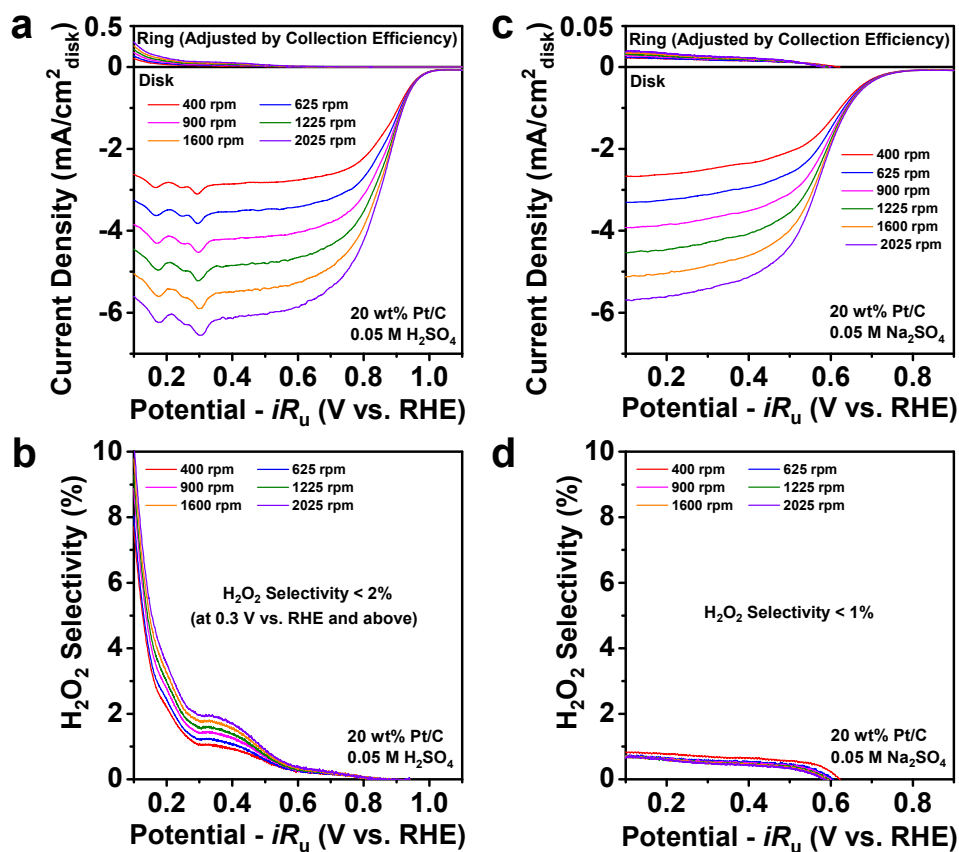
Figure S5. RRDE measurements and the corresponding H_2O_2 selectivity of drop-casted Pt/C in O_2-saturated (a,b) 0.05 M H_2SO_4 and (c,d) 0.05 M Na_2SO_4. Very low H_2O_2 selectivity was observed in both acidic and neutral solution (Pt/C is a known $4e^-$ ORR catalyst), showing that 1.3 V vs. RHE is an appropriate ring potential (without triggering water oxidation) for RRDE measurements in both acidic and neutral solutions**.**
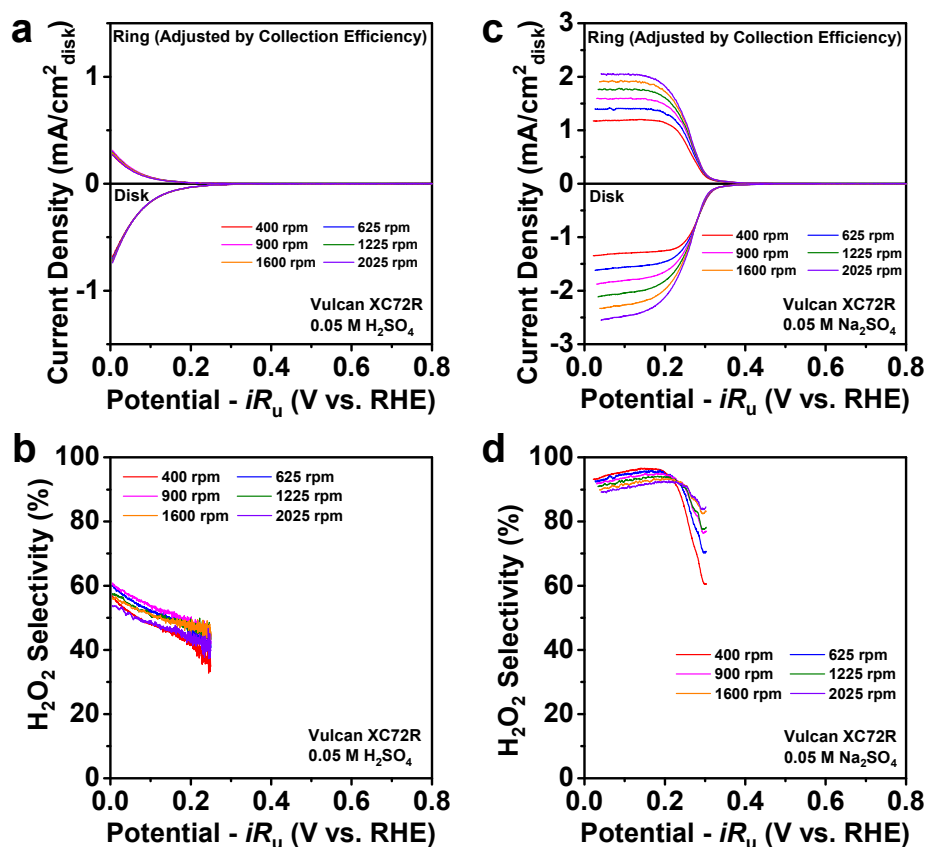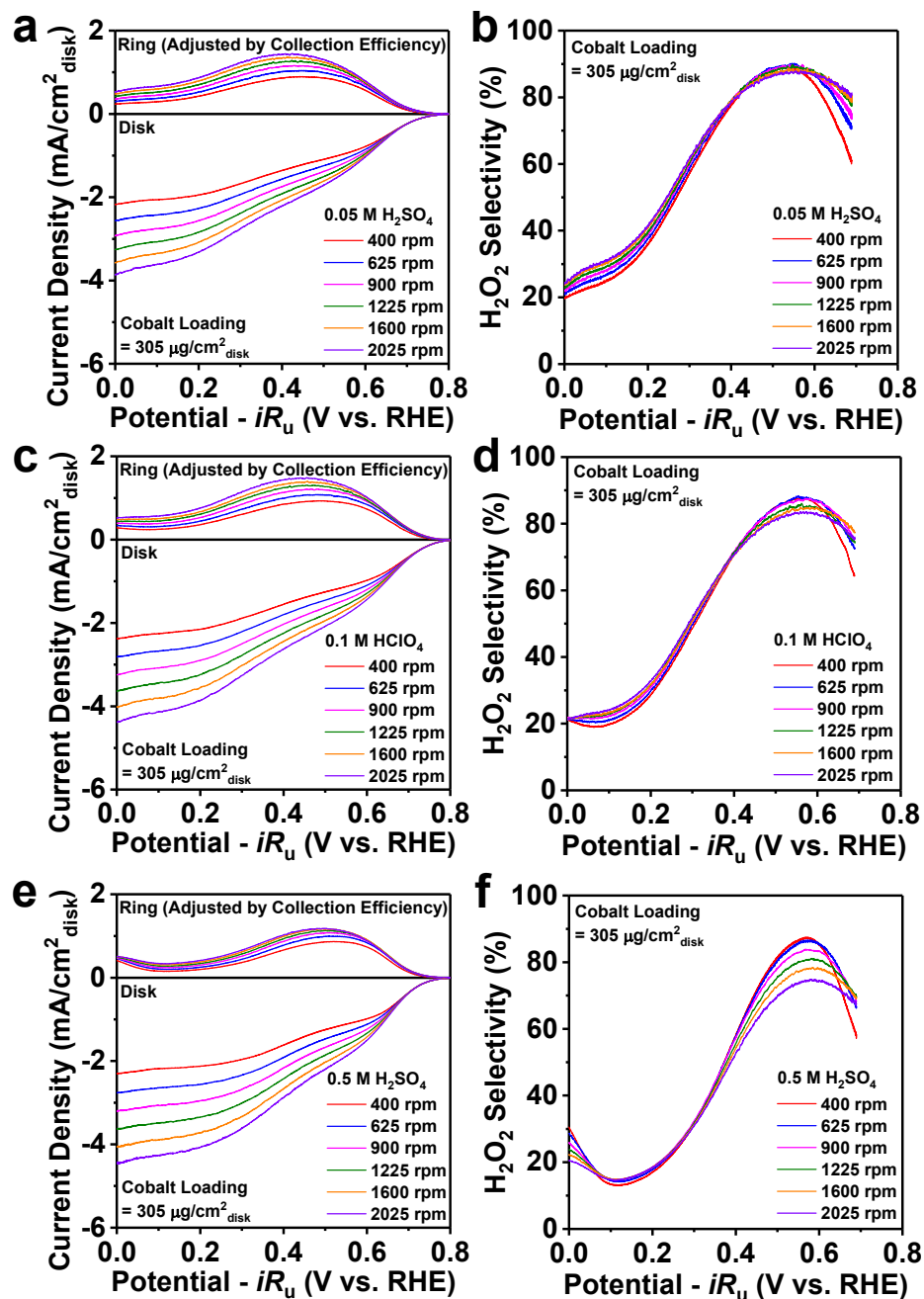
Figure S6. RRDE measurements and the corresponding H_2O_2 selectivity of drop-casted Vulcan carbon black in O_2-saturated (a,b) 0.05 M H_2SO_4 and (c,d) 0.05 M Na_2SO_4. Considerable H_2O_2 selectivity was observed in both acidic and neutral solution (Vulcan carbon black is moderately selective towards 2e$^-$ ORR but has a poor catalytic activity), showing that 1.3 V vs. RHE is an appropriate ring potential (driving fast H_2O_2 oxidation) for RRDE measurements in both acidic and neutral solutions.

Figure S7. RRDE measurements and the corresponding H_2O_2 selectivity of drop-casted CoS_2 (cobalt loading = 305 $\mu g/cm^2_{disk}$) in O_2-saturated (a,b) 0.05 M H_2SO_4 (pH 1.21), (c,d) 0.1 M $HClO_4$ (pH 1.02), and (e,f) 0.5 M H_2SO_4 (pH 0.35).
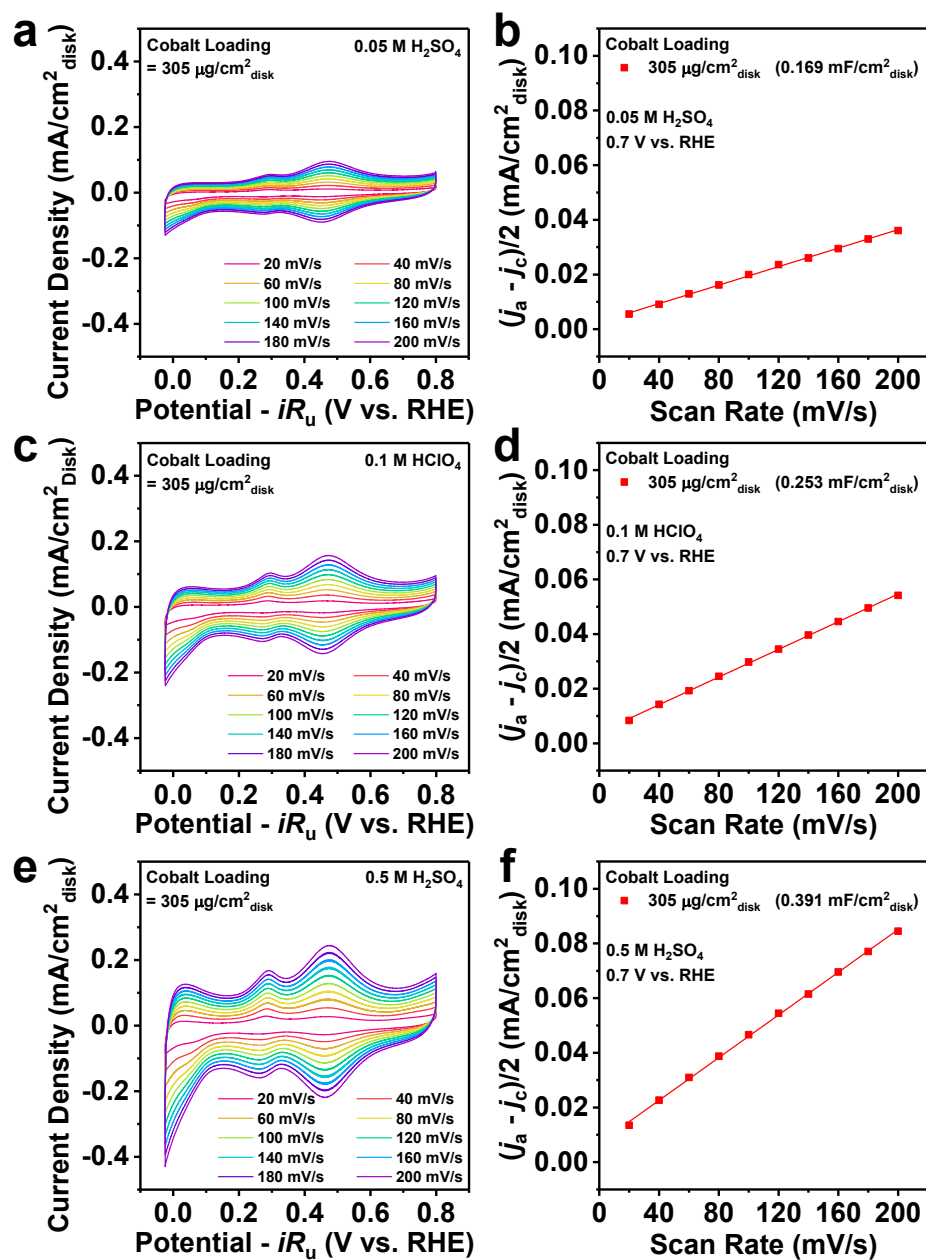
Figure S8. Electrochemically active surface area (ECSA) measurements of drop-casted CoS$_2$ (cobalt loading = 305 μg/cm$^2_{disk}$) in Ar-saturated (a,b) 0.05 M H$_2$SO$_4$, (c,d) 0.1 M HClO$_4$, and (e,f) 0.5 M H$_2$SO$_4$. RRDE measurements were shown in Figure S7. Double-layer capacitances (C$_{dl}$) were determined at 0.7 V vs. RHE in all cases to avoid the interference of Faradaic currents.
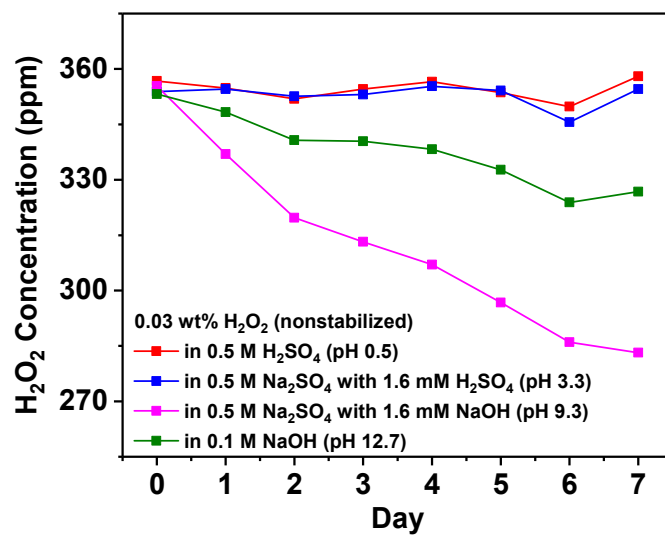
Figure S9. Chemical stability of nonstabilized H_2O_2 under different pH conditions, showing a higher decomposition rate of H_2O_2 in alkaline solution compared with that in acidic solution which is negligible over the time period of one week.
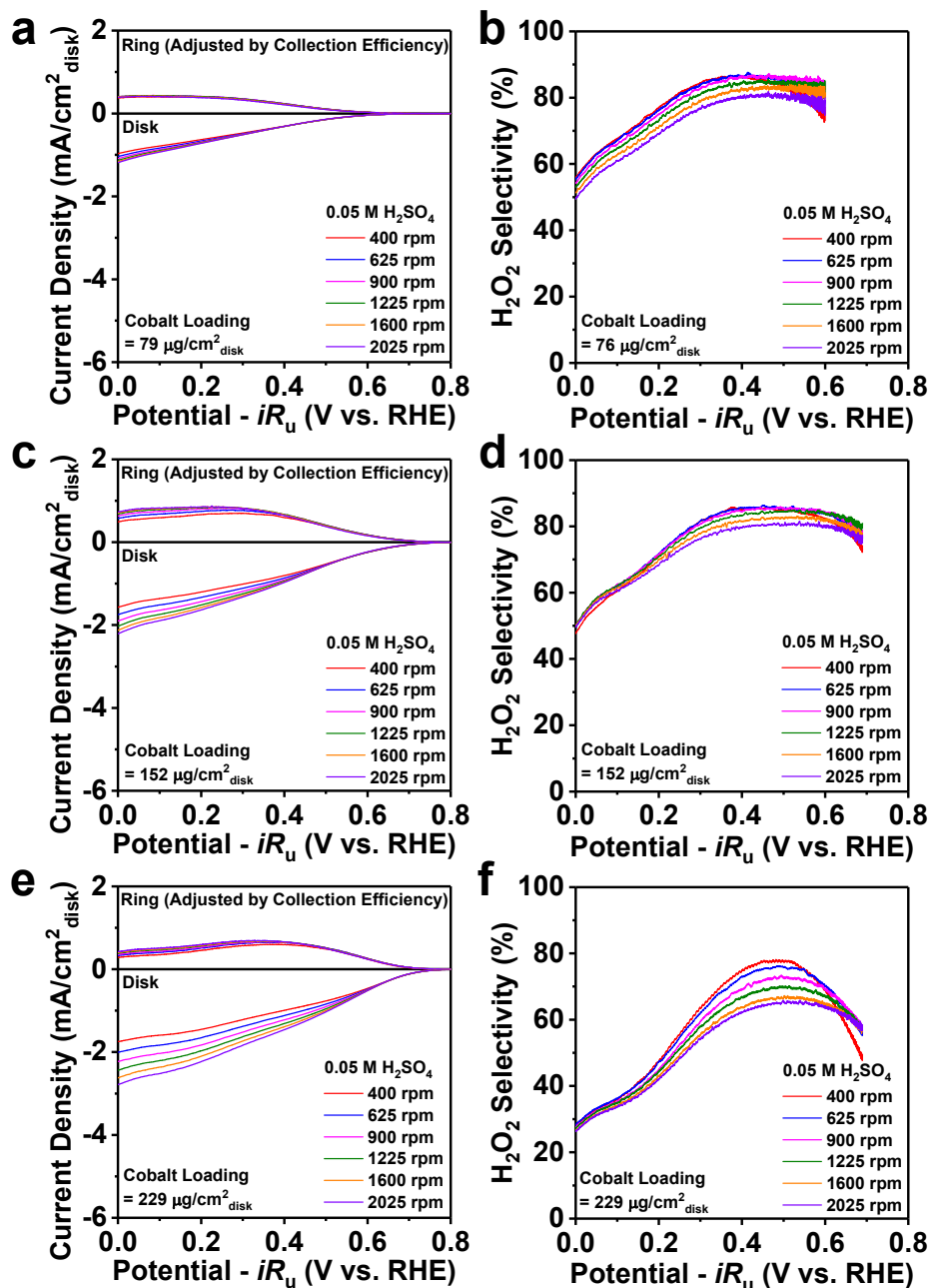
Figure S10. RRDE measurements and the corresponding H_2O_2 selectivity of drop-casted CoS_2 in O_2-saturated 0.05 M H_2SO_4 with various cobalt loadings: (a,b) 76 μg/cm$^2_{disk}$, (c,d) 152 μg/cm$^2_{disk}$, and (e,f) 229 μg/cm$^2_{disk}$.
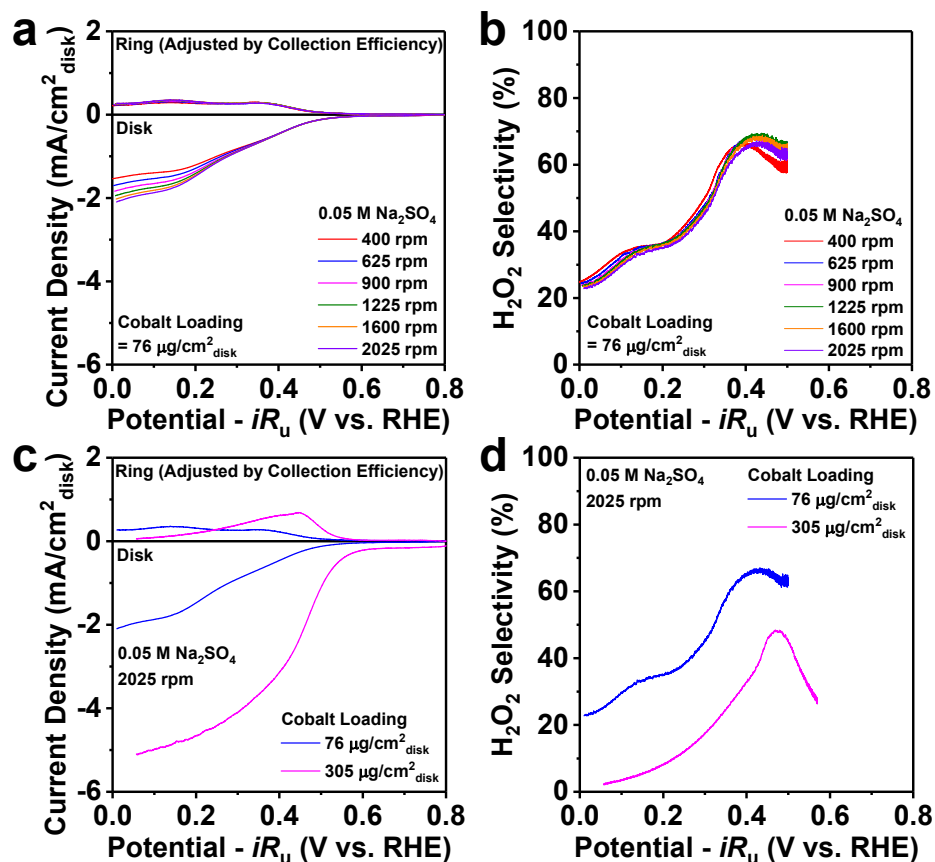
Figure S11. (a) RRDE measurements and (b) the corresponding H_2O_2 selectivity of drop-casted CoS_2 (cobalt loading = 76 $\mu g/cm^2_{disk}$) in O_2-saturated 0.05 M Na_2SO_4. Comparisons of (c) RRDE voltammograms at 2025 rpm and (d) H_2O_2 selectivity at different cobalt loadings.
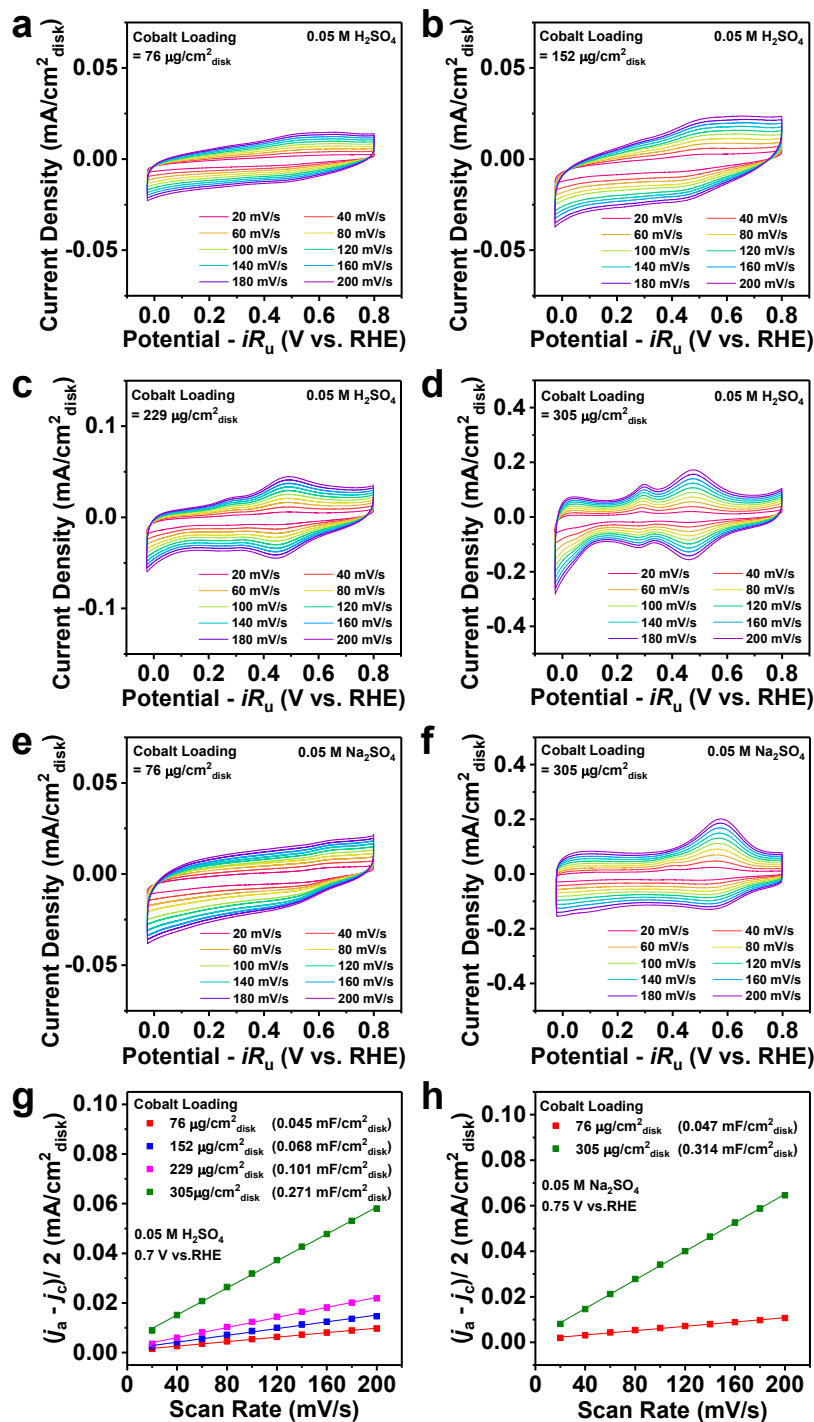
Figure S12. Electrochemically active surface area (ECSA) measurements of drop-casted CoS$_2$ at different cobalt loadings in Ar-saturated (a-d) 0.05 M H$_2$SO$_4$ and (e,f) 0.05 M Na$_2$SO$_4$. RRDE measurements were shown in Figure 2, S10, S11. Double-layer capacitances (C_{dl}) were determined at (g) 0.7 V vs. RHE in 0.05 M H$_2$SO$_4$ and (h) 0.75 V vs. RHE in 0.05 M Na$_2$SO$_4$, respectively, to avoid the interference of Faradaic currents.
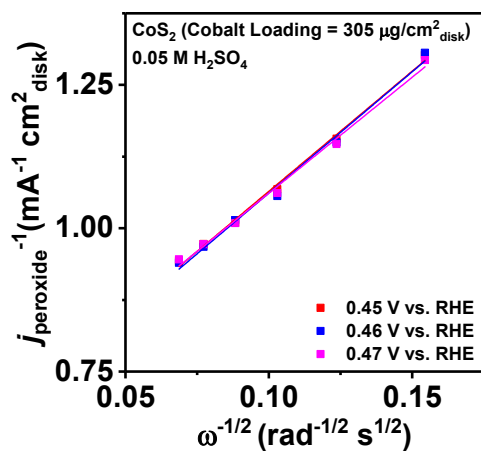
Figure S13. Koutecky-Levich (K-L) analysis of the hydrogen peroxide current density (j_{peroxide}) of drop-casted CoS_2 (cobalt loading = 305 $\mu g/cm^2_{\text{disk}}$) in O_2-saturated 0.05 M H_2SO_4 (RRDE voltammograms shown in Figure 2a). The K-L analysis was performed around 0.46 V vs. RHE where the maximum j_{peroxide} was reached (see Table S2 for detailed analysis).
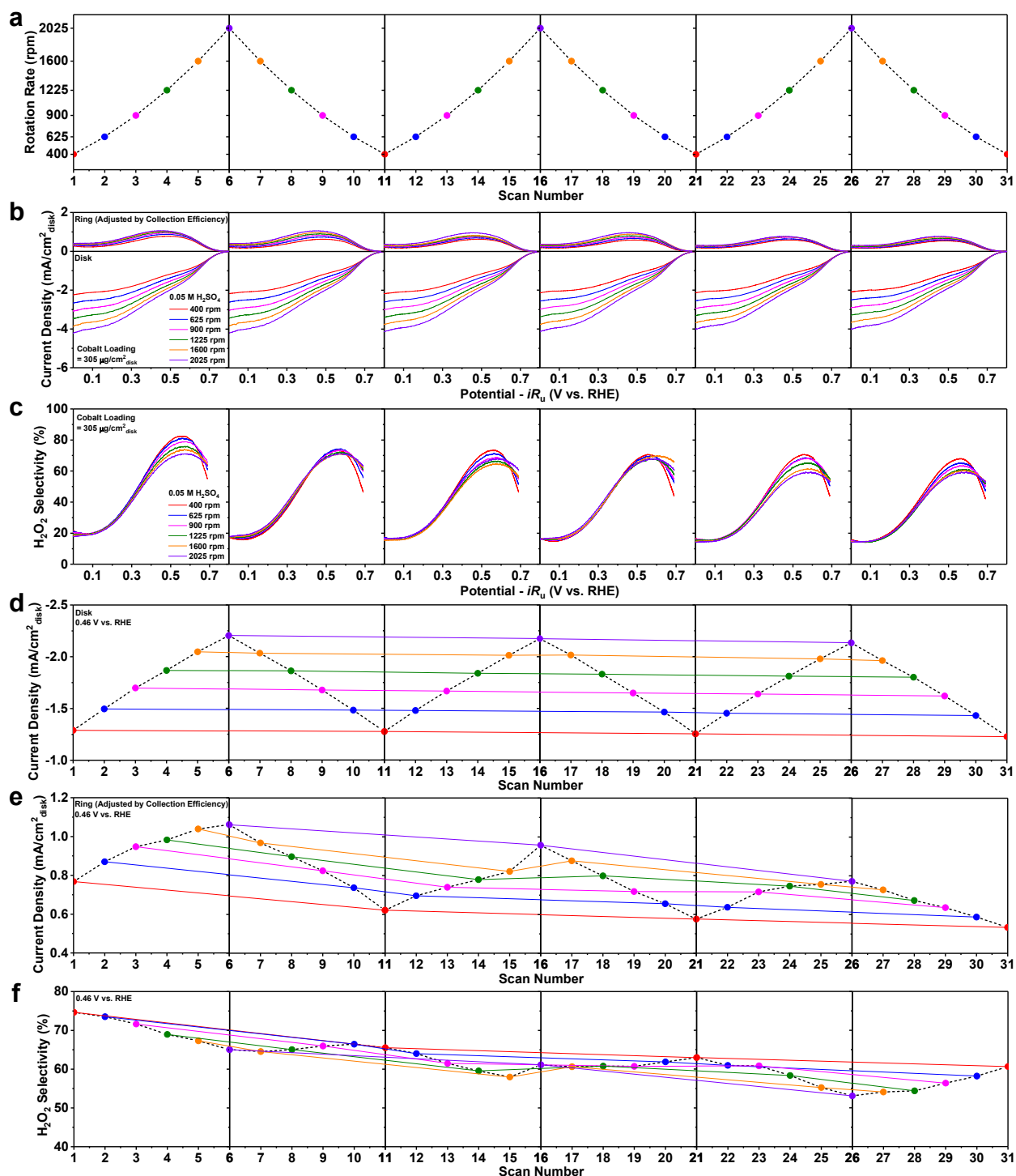
Figure S14. ORR operational stability test of drop-casted CoS_2 in O_2-saturated 0.05 M H_2SO_4. (a) RRDE scan profile, (b) RRDE voltammograms, and (c) the corresponding H_2O_2 selectivity. Time evolution of (d) the disk current density, (e) the ring current density, and (f) the corresponding H_2O_2 selectivity at the disk potential of 0.46 V vs. RHE (after *iR*-correction).

Figure S15. ORR operational stability tests of drop-casted CoS_2 in O_2-saturated 0.05 M Na_2SO_4. (a) RRDE scan profile, (b) RRDE voltammograms, and (c) the corresponding H_2O_2 selectivity. Time evolution of (d) the disk current density, (e) the ring current density, and (f) the corresponding H_2O_2 selectivity at the disk potential of 0.46 V vs. RHE (after *iR*-correction).
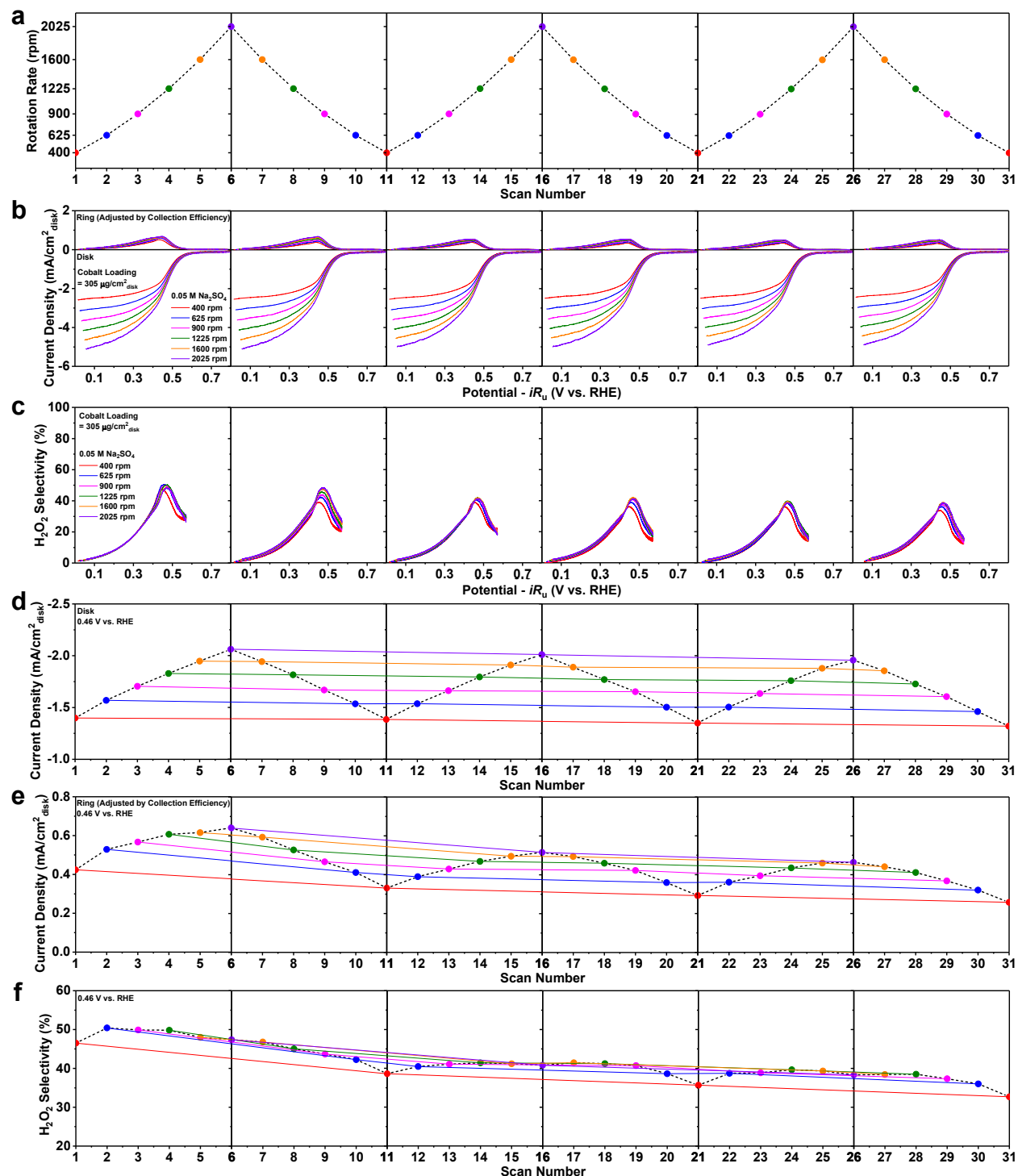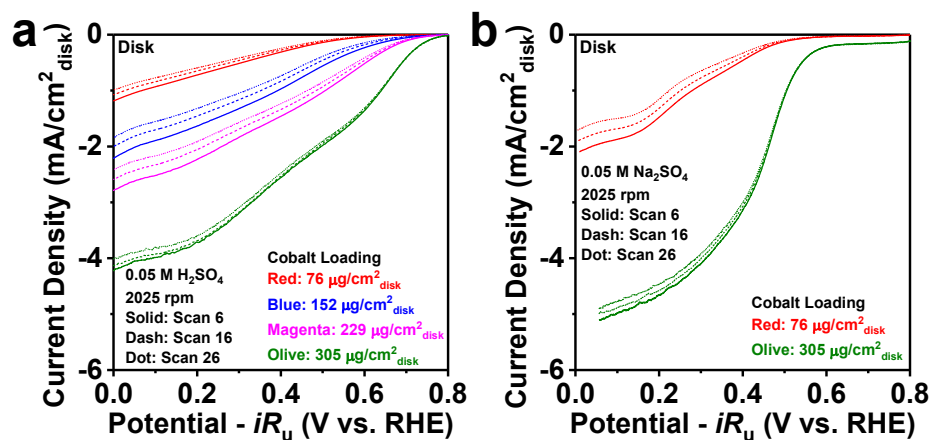
Figure S16. Time evolution of the disk current density at 2025 rpm during ORR operational stability tests of drop-casted CoS_2 with various cobalt loadings in O_2-saturated (a) 0.05 M H_2SO_4 and (b) 0.05 M Na_2SO_4.
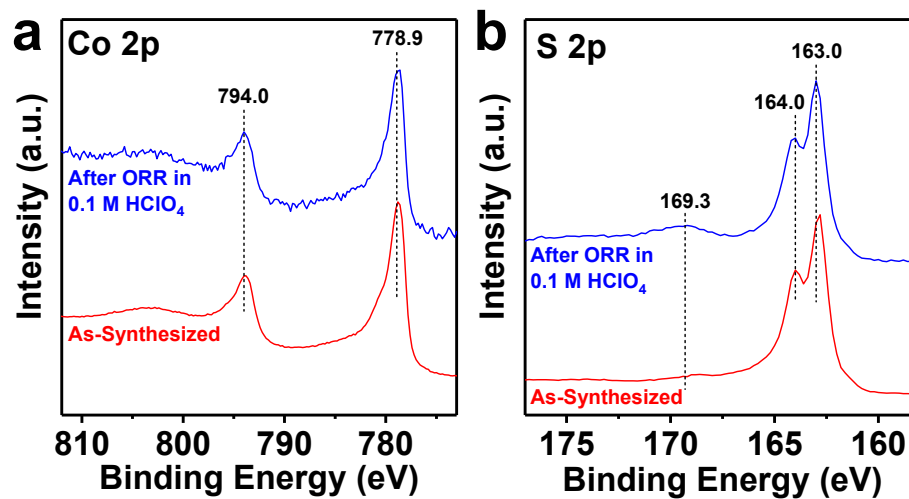
Figure S17. (a) Co 2p and (b) S 2p XPS spectra of drop-casted CoS$_2$ before and after operational stability tests in O$_2$-saturated 0.1 M HClO$_4$.
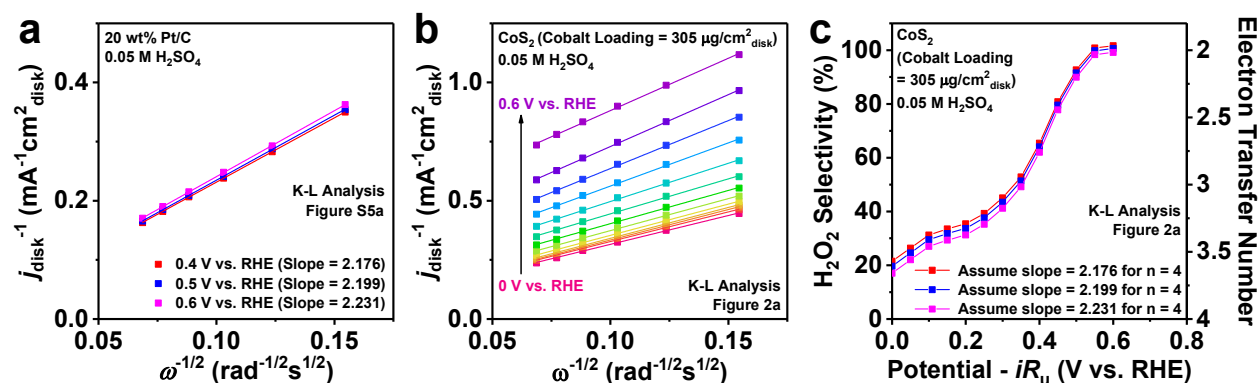
Figure S18. (a) Koutecky-Levich (K-L) analysis of drop-casted Pt/C in O₂-saturated 0.05 M H₂SO₄, where the limiting current for the 4e⁻ ORR (~6 mA/cm²$_{disk}$ at 1600 rpm) was achieved. (b) K-L analysis and (c) the corresponding H₂O₂ selectivity and electron transfer number (*n*) of drop-casted CoS₂ (cobalt loading = 305 μg/cm²$_{disk}$) in O₂-saturated 0.05 M H₂SO₄. RRDE voltammograms of Pt/C and CoS₂ were shown in Figure S5a and 2a, respectively. The K-L slopes of Pt/C at different potentials were used as internal standards of the 4e⁻ ORR (*n* = 4) for the K-L analysis of CoS₂ (see Table S4 for details).
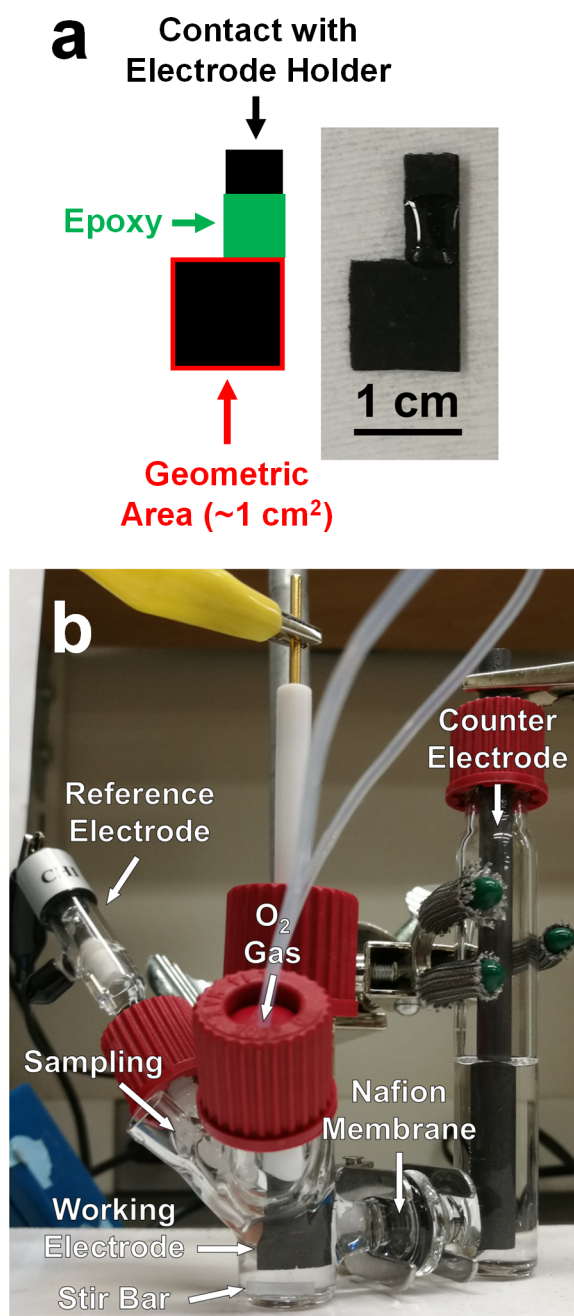
Figure S19. (a) Schematic and digital photograph of CoS$_2$/CFP working electrodes. (b) Digital photograph of the three-electrode H-cell setup (with key components labeled) for the bulk electrocatalytic production of H$_2$O$_2$.
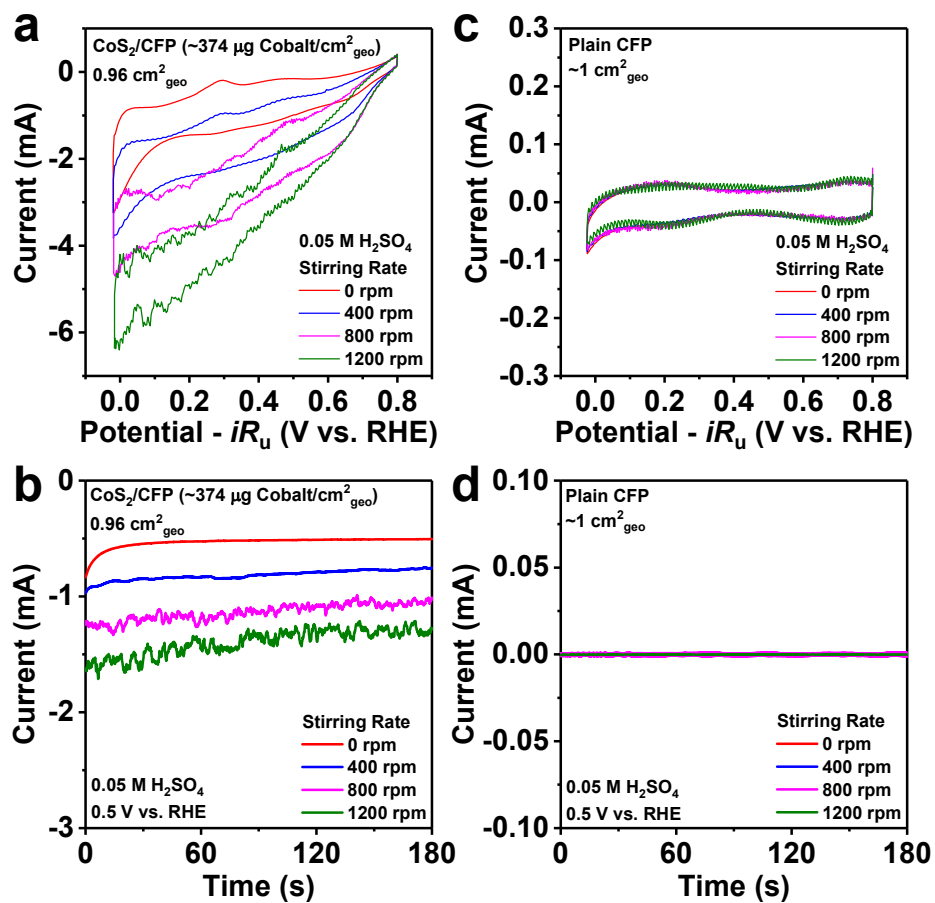
Figure S20. CV voltammograms (at 100 mV/s) and chronoamperometry tests (at 0.5 V vs. RHE) of (a,b) CoS$_2$/CFP and (c,d) plain CFP in O$_2$-saturated 0.05 M H$_2$SO$_4$ at different stir rates using the three-electrode H-cell setup.
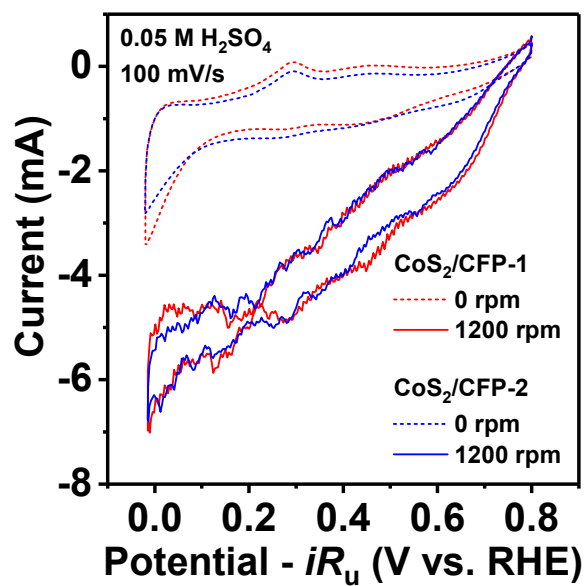
Figure S21. CV voltammograms (at 100 mV/s) of two CoS2/CFP working electrodes (shown in Figure 6) in O2-saturated 0.05 M H2SO4 at 0 and 1200 rpm stir rates using the three-electrode H-cell setup.
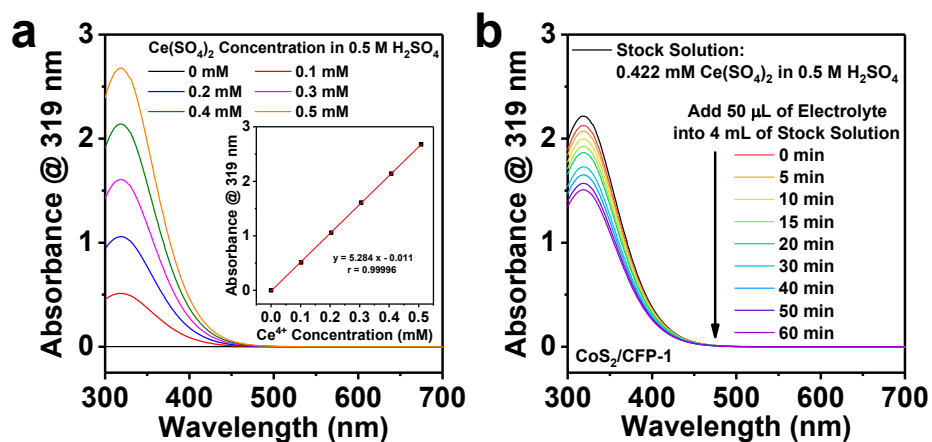
Figure S22. (a) Absorbance spectra of standard Ce(SO₄)₂ solutions (up to 0.5 mM) in 0.5 M H₂SO₄, generating a linear calibration curve (shown as an inset) at the peak wavelength (319 nm). (b) Absorbance spectra of Ce(SO₄)₂ stock solution (0.422 mM, determined from calibration curve) in 0.5 M H₂SO₄ before and after injecting aliquot of electrolyte taken out of the working electrode compartment at specific time intervals during electrolysis.

Figure S23. PXRD pattern of the as-synthesized CoS$_2$/CFP and the post-electrolysis CoS$_2$/CFP-1 electrode (shown in Figure 6) in comparison with the standard PXRD pattern of CoS$_2$ (JCPDS #41-1471). The peaks marked with asterisks come from carbon fiber paper.

Table S1. Preparation and electrochemically active surface area (ECSA) of drop-casted CoS$_2$ on RRDE.

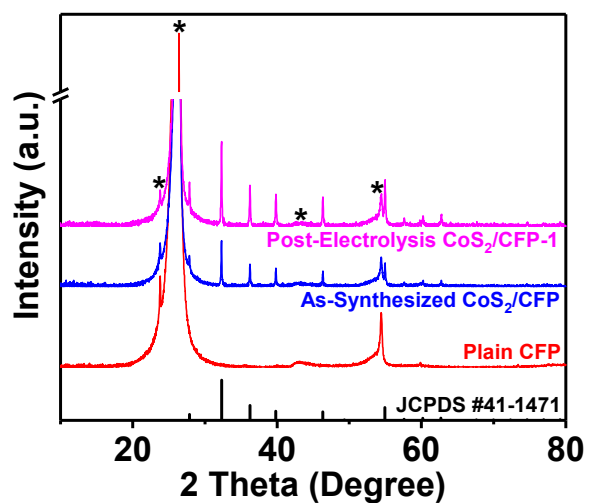| Electrolyte	CoS$_2$ Mass	5 wt% Nafion Volume	Water Volume	Drop-Cast Volume	Cobalt Loading	Nafion Loading	Double-Layer Capacitance[a]
0.05 M H$_2$SO$_4$	5.2 mg	2340 µL	260 µL	10 µL	76 µg/cm$^2_{disk}$	191 µg/cm$^2_{disk}$	0.045 mF/cm$^2_{disk}$
	5.0 mg	1125 µL	125 µL	10 µL	152 µg/cm$^2_{disk}$	191 µg/cm$^2_{disk}$	0.068 mF/cm$^2_{disk}$
	5.2 mg	780 µL	87 µL	10 µL	229 µg/cm$^2_{disk}$	191 µg/cm$^2_{disk}$	0.101 mF/cm$^2_{disk}$
	5.1 mg	574 µL	64 µL	10 µL	305 µg/cm$^2_{disk}$	191 µg/cm$^2_{disk}$	0.271 mF/cm$^2_{disk}$
0.05 M Na$_2$SO$_4$	5.3 mg	2385 µL	265 µL	10 µL	76 µg/cm$^2_{disk}$	191 µg/cm$^2_{disk}$	0.047 mF/cm$^2_{disk}$
	5.0 mg	562 µL	63 µL	10 µL	305 µg/cm$^2_{disk}$	192 µg/cm$^2_{disk}$	0.314 mF/cm$^2_{disk}$

[a] Double-layer capacitances were determined at 0.7 V vs. RHE in 0.05 M H$_2$SO$_4$ and 0.75 V vs. RHE in 0.05 M Na$_2$SO$_4$, respectively, to avoid the interference of Faradaic currents (see Figure S12).

Table S2. Koutecky-Levich (K-L) analysis of the hydrogen peroxide current density ($j_{peroxide}$) of drop-casted CoS_2 (cobalt loading = 305 $\mu g/cm^2_{disk}$) in O_2-saturated 0.05 M H_2SO_4 (RRDE voltammograms shown in Figure 2a). The K-L analysis was performed around 0.46 V vs. RHE where the maximum $j_{peroxide}$ was reached.

Catalyst	Potential (V vs. RHE)	Slope of $j_{peroxide}^{-1}$ vs. $\omega^{-1/2}$ ($mA^{-1}\,cm^2_{disk}\,rad^{1/2}\,s^{-1/2}$)	$j_{k,peroxide}$ ($mA\,cm^{-2}_{disk}$)	$j_{L,peroxide}$ at 1600 rpm ($mA\,cm^{-2}_{disk}$)	r^2
CoS_2 (cobalt loading = 305 $\mu g/cm^2_{disk}$) (Figure 2a)	0.45	4.191	1.550	3.089	0.995
	0.46	4.232	1.567	3.059	0.989
	0.47	4.047	1.523	3.198	0.992

Equations:

$$j_{disk} = \frac{i_{disk}}{A_{disk}}$$

$$j_{ring} = \frac{i_{ring}}{A_{disk} \times N} = j_{peroxide}$$

$$\frac{1}{j_{peroxide}} = \frac{1}{j_{k,peroxide}} + \frac{1}{j_{L,peroxide}}$$

$$\frac{1}{j_{peroxide}} = \frac{1}{j_{k,peroxide}} + B \times \omega^{-1/2}$$

$$j_{L,peroxide} = \frac{1}{B} \times \omega^{1/2}$$

where $j_{peroxide}$ is the hydrogen peroxide current density, $j_{k,peroxide}$ is the kinetic current density for H_2O_2 production, $j_{L,peroxide}$ is the diffusion-limited current density for H_2O_2 production, B is the slope of $j_{peroxide}^{-1}$ vs. $\omega^{-1/2}$.

Explanations:

1. We confirmed that the Koutecky-Levich equation is applicable to the hydrogen peroxide current density given the good linearity of $j_{peroxide}^{-1}$ vs. $\omega^{-1/2}$ (Figure S13).

2. We calculated $j_{L,peroxide}$ at 1600 rpm ($j_{L,peroxide} = \frac{1}{B} \times \omega^{1/2}$) and found it in good agreement with the theoretical limiting current density for 2e$^-$ ORR (~3 mA/cm$^2_{disk}$ at 1600 rpm, see Table S2). Therefore, we used $j_{L,peroxide} = 3$ mA/cm$^2_{disk}$ to correct for mass-transport loss.

3. We used the equation $j_{k,peroxide} = \frac{j_{peroxide} \times j_{L,peroxide}}{j_{L,peroxide} - j_{peroxide}} = \frac{j_{peroxide} \times 3\,mA/cm^2_{disk}}{3\,mA/cm^2_{disk} - j_{peroxide}}$ to correct for mass-transport loss in the hydrogen peroxide current density of drop-casted CoS_2 (cobalt loading = 305 $\mu g/cm^2_{disk}$) in 0.05 M H_2SO_4 at the rotation rate of 1600 rpm (RRDE voltammograms shown in Figure 2a), yielding a plot of $j_{k,peroxide}$ vs. potential (shown in Figure 4).

Table S3. Summary of RRDE electrode information of CoS_2 and other reported ORR electrocatalysts for H_2O_2 production in acidic solution.

Classification	Catalyst	Electrolyte; Scan Rate; Rotation Rate; Ring Potential	Electrode Preparation	Geometric Area of GC Disk	Surface Area of Catalyst	Catalyst Loading	Reference
Earth-abundant transition metal compounds	CoS_2 nanomaterials	0.05 M H_2SO_4; 50 mV/s; 1600 rpm; 1.3 V vs. RHE	CoS_2 drop-casted on RRDE (GC disk-Pt-ring)	0.126 cm^2_{disk}	Not mentioned	305 ug Co/cm^2_{disk}	This work
Noble metal nanoparticles (NPs)	Pd-Au NPs (Au_3Pd)	0.1 M $HClO_4$; 50 mV/s; 900 rpm; 1.28 V vs. RHE	Pd-Au NPs drop-casted on RRDE (GC disk-Pt-ring)	0.196 cm^2_{disk}	surface area of Pd-Au NPs 1.93 cm^2	10 ug total metal/cm^2_{disk} (7.7 ug Au/cm^2_{disk}) (2.3 ug Pd/cm^2_{disk})	Ref. S4
	Pt-Hg NPs/C (Pt core, $PtHg_4$ shell)	0.1 M $HClO_4$; 50 mV/s; 1600 rpm; 1.2 V vs. RHE	60 wt% Pt NPs/C drop-casted on RRDE (GC disk-Pt-ring); Hg electrodeposition into Pt NPs	0.196 cm^2_{disk}	surface area of Pt NPs 1.07 ± 0.06 cm^2	14 ug Pt/cm^2_{disk}	Ref. S5
	Pd-Hg NPs/C (Pd core, Pd_2Hg_5 shell)	0.1 M $HClO_4$; 50 mV/s; 1600 rpm; 1.2 V vs. RHE	60 wt% Pd NPs/C drop-casted on RRDE (GC disk-Pt-ring); Hg electrodeposition into Pd NPs	0.196 cm^2_{disk}	surface area of Pd NPs 1.11 ± 0.04 cm^2	10 ug Pd/cm^2_{disk}	Ref. S6
Noble metal polycrystalline extended surfaces (pc)	Pt-Hg (pc) ($PtHg_4$ surface)	0.1 M $HClO_4$; 50 mV/s; 1600 rpm; 1.2 V vs. RHE	Pt disk-Pt ring RRDE; Hg electrodeposition into Pt disk	0.196 cm^2_{disk}	surface area of Pt disk 0.196 cm^2	Not applicable	Ref. S5
	Pd-Hg (pc) (Pd_2Hg_5 surface)	0.1 M $HClO_4$; 50 mV/s; 1600 rpm; 1.2 V vs. RHE	Pd disk-Pt ring RRDE; Hg electrodeposition into Pd disk	0.196 cm^2_{disk}	surface area of Pd disk 0.196 cm^2	Not applicable	Ref. S6
	Ag (pc)	0.1 M $HClO_4$; 50 mV/s; 1600 rpm; 1.2 V vs. RHE	Ag disk-Pt ring RRDE	0.196 cm^2_{disk}	surface area of Ag disk 0.196 cm^2	Not applicable	Ref. S6
	Ag-Hg (pc)	0.1 M $HClO_4$; 50 mV/s; 1600 rpm; 1.2 V vs. RHE	Ag disk-Pt ring RRDE; Hg electrodeposition into Ag disk	0.196 cm^2_{disk}	surface area of Ag disk 0.196 cm^2	Not applicable	Ref. S6
	Cu-Hg (pc) (Cu_2Hg_5 surface)	0.1 M $HClO_4$; 50 mV/s; 1600 rpm; 1.2 V vs. RHE	Cu disk-Pt ring RRDE; Hg electrodeposition into Cu disk	0.196 cm^2_{disk}	surface area of Cu disk 0.196 cm^2	Not applicable	Ref. S6
Carbon materials	Nitrogen-doped carbon (N/C)	0.1 M $HClO_4$; 5 mV/s; 1600 rpm; 1.2 V vs. RHE	N/C drop-casted on RRDE (GC disk-Pt ring)	0.196 cm^2_{disk}	Not mentioned	310 ug catalyst/cm^2_{disk}	Ref. S7
Single-atom noble metal catalysts	5 wt% single-atom Pt on sulfur-doped carbon (Pt_1/SC)	0.1 M $HClO_4$; 10 mV/s; 900 rpm; 1.2 V vs. RHE	Pt_1/SC drop-casted on RRDE (GC disk-Pt ring)	0.126 cm^2_{disk}	Not mentioned	50 ug catalyst/cm^2_{disk} (2.5 ug Pt/cm^2_{disk})	Ref. S8
	0.35 wt% single-atom Pt on TiN (Pt_1/TiN)	0.1 M $HClO_4$; 10 mV/s; 1600 rpm; 1.2 V vs. RHE	Pt_1/TiN and carbon black drop-casted on RRDE (GC disk-Pt ring)	Not mentioned	Not mentioned	15 ug catalyst (0.052 ug Pt)	Ref. S9
	24.8 at% single-atom Pt on hollow CuS_x (h-Pt_1-CuS_x)	0.1 M $HClO_4$; Not mentioned; 1600 rpm; 1.1 V vs. RHE	h-Pt_1-CuS_x supported on carbon black (Pt loading ~15 wt%) drop-casted on RRDE (GC disk-Pt ring)	0.2475 cm^2_{disk}	Not mentioned	101 ug catalyst/cm^2_{disk} (15.2 ug Pt/cm^2_{disk})	Ref. S10
Porphyrin-like structures	Heat-treated 0.3 wt% Co-porphyrin on carbon black (Co-N/C)	0.6 M H_2SO_4; 20 mV/s; 1600 rpm; ~1.3 V vs. RHE	Co-N/C drop-casted on RRDE (GC disk-Pt ring)	0.071 cm^2_{disk}	Not mentioned	1 mg catalyst/cm^2_{disk} (3 ug Co/cm^2_{disk})	Ref. S11

Table S4. Koutecky-Levich analysis of drop-casted Pt/C and CoS$_2$ (cobalt loading = 305 µg/cm$^2_{disk}$) in O$_2$-saturated 0.05 M H$_2$SO$_4$. RRDE voltammograms of Pt/C and CoS$_2$ (cobalt loading = 305 µg/cm$^2_{disk}$) were presented in Figure S5a and Figure 2a, respectively.

Catalyst	Potential (V vs. RHE)	Slope of j_{disk}^{-1} vs. $\omega^{-1/2}$ (mA^{-1} cm$^2_{disk}$ rad$^{1/2}$ s$^{-1/2}$)	r^2
Pt/C (Figure S5a)	0.40	2.176	0.99997
	0.50	2.199	0.99987
	0.60	2.231	0.99994
CoS$_2$ (cobalt loading = 305 µg/cm$^2_{disk}$) (Figure 2a)	0	2.438	0.9988
	0.05	2.507	0.9992
	0.10	2.579	0.9995
	0.15	2.614	0.9994
	0.20	2.644	0.9996
	0.25	2.708	0.9994
	0.30	2.809	0.9988
	0.35	2.958	0.9979
	0.40	3.234	0.9983
	0.45	3.651	0.9985
	0.50	4.055	0.9989
	0.55	4.389	0.9993
	0.60	4.426	0.9984

Table S5. Comparisons of the bulk electrocatalytic H_2O_2 production performance of CoS_2/CFP with the benchmark Pt-Hg alloy catalyst.

Catalyst	Electrolyte	Electrolysis Potential	Electrolysis Time	Cumulative Charge	Cumulative H_2O_2 Yield	Cumulative H_2O_2 Concentration	Cumulative H_2O_2 Selectivity	Cumulative Faradaic Efficiency
CoS_2/CFP[a]	0.05 M H_2SO_4 (3 mL)	0.5 V vs. RHE	5 min	0.563 C	1.23 μmol	0.41 mM	59.3%	42.1%
			10 min	1.046 C	2.88 μmol	0.96 mM	69.4%	53.1%
			15 min	1.532 C	4.44 μmol	1.48 mM	71.7%	55.9%
			20 min	*2.021 C*	*5.72 μmol*	*1.91 mM*	*70.6%*	*54.6%*
			30 min	2.994 C	8.60 μmol	2.87 mM	71.3%	55.4%
			40 min	3.968 C	10.20 μmol	3.40 mM	66.3%	49.6%
			50 min	5.006 C	11.87 μmol	3.96 mM	62.8%	45.8%
			60 min	*6.125 C*	*13.08 μmol*	*4.36 mM*	*58.4%*	*41.2%*
Pt-Hg Alloy[b]	0.1 M $HClO_4$ (15 mL)	0.4 V vs. RHE	4.2 min	0.500 C	2.49 μmol	0.17 mM	98.0%	96.1%
			7.1 min	0.836 C	3.01 μmol	0.20 mM	82.1%	69.5%
			9.2 min	1.056 C	4.50 μmol	0.30 mM	90.3%	82.3%
			18.3 min	*2.034 C*	*7.00 μmol*	*0.47 mM*	*79.8%*	*66.4%*

[a] All numerical data for the electrocatalytic H_2O_2 production performance of CoS_2/CFP are based on the CoS_2/CFP-1 electrode (shown in Figure 6).

[b] All numerical data for the electrocatalytic H_2O_2 production performance of the Pt-Hg alloy catalyst were estimated from the published figures (Figure S24 in ref. S5).

SUPPORTING REFERENCES

S1.   Faber, M. S.; Dziedzic, R.; Lukowski, M. A.; Kaiser, N. S.; Ding, Q.; Jin, S. High-Performance Electrocatalysis Using Metallic Cobalt Pyrite (CoS_2) Micro- and Nanostructures. *J. Am. Chem. Soc.* **2014,** *136*, 10053-10061.

S2.   Stevens, M. B.; Enman, L. J.; Batchellor, A. S.; Cosby, M. R.; Vise, A. E.; Trang, C. D. M.; Boettcher, S. W. Measurement Techniques for the Study of Thin Film Heterogeneous Water Oxidation Electrocatalysts. *Chem. Mater.* **2017,** *29*, 120-140.

S3.   Bouchaud, B.; Balmain, J.; Bonnet, G.; Pedraza, F. pH-Distribution of Cerium Species in Aqueous Systems. *J. Rare Earth.* **2012,** *30*, 559-562.

S4.   Pizzutilo, E.; Kasian, O.; Choi, C. H.; Cherevko, S.; Hutchings, G. J.; Mayrhofer, K. J. J.; Freakley, S. J. Electrocatalytic Synthesis of Hydrogen Peroxide on Au-Pd Nanoparticles: From Fundamentals to Continuous Production. *Chem. Phys. Lett.* **2017,** *683*, 436-442.

S5.   Siahrostami, S.; Verdaguer-Casadevall, A.; Karamad, M.; Deiana, D.; Malacrida, P.; Wickman, B.; Escudero-Escribano, M.; Paoli, E. A.; Frydendal, R.; Hansen, T. W.; Chorkendorff, I.; Stephens, I. E. L.; Rossmeisl, J. Enabling Direct H_2O_2 Production through Rational Electrocatalyst Design. *Nat. Mater.* **2013,** *12*, 1137-1143.

S6.   Verdaguer-Casadevall, A.; Deiana, D.; Karamad, M.; Siahrostami, S.; Malacrida, P.; Hansen, T. W.; Rossmeisl, J.; Chorkendorff, I.; Stephens, I. E. L. Trends in the Electrochemical Synthesis of H_2O_2: Enhancing Activity and Selectivity by Electrocatalytic Site Engineering. *Nano Lett.* **2014,** *14*, 1603-1608.

S7.   Hasché, F.; Oezaslan, M.; Strasser, P.; Fellinger, T.-P. Electrocatalytic Hydrogen Peroxide Formation on Mesoporous Non-Metal Nitrogen-Doped Carbon Catalyst. *J. Energy Chem.* **2016,** *25*, 251-257.

S8.   Choi, C. H.; Kim, M.; Kwon, H. C.; Cho, S. J.; Yun, S.; Kim, H.-T.; Mayrhofer, K. J. J.; Kim, H.; Choi, M. Tuning Selectivity of Electrochemical Reactions by Atomically Dispersed Platinum Catalyst. *Nat. Commun.* **2016,** *7*, 10922.

S9.   Yang, S.; Kim, J.; Tak, Y. J.; Soon, A.; Lee, H. Single-Atom Catalyst of Platinum Supported on Titanium Nitride for Selective Electrochemical Reactions. *Angew. Chem. Int. Ed.* **2016,** *55*, 2058-2062.

S10.   Shen, R.; Chen, W.; Peng, Q.; Lu, S.; Zheng, L.; Cao, X.; Wang, Y.; Zhu, W.; Zhang, J.; Zhuang, Z.; Chen, C.; Wang, D.; Li, Y. High-Concentration Single Atomic Pt Sites on Hollow CuS_x for Selective O_2 Reduction to H_2O_2 in Acid Solution. *Chem* **2019,** *5*, 2099-2110.

S11.   Yamanaka, I.; Ichihashi, R.; Iwasaki, T.; Nishimura, N.; Murayama, T.; Ueda, W.; Takenaka, S. Electrocatalysis of Heat-Treated Cobalt-Porphyrin/Carbon for Hydrogen Peroxide Formation. *Electrochim. Acta* **2013,** *108*, 321-329.